Full Paper
doi.org/10.1002/chem.202001643

Marcasite Materials

Chemical Bonding in Colossal Thermopower $FeSb_2$

Thomas Bjørn Egede Grønbech,[a] Kasper Tolborg,[a] Helle Svendsen,[a] Jacob Overgaard,[a] Yu-Sheng Chen,[b] and Bo Brummerstedt Iversen*[a]

Abstract: $FeSb_2$ exhibits a colossal Seebeck coefficient (S) and a record-breaking high thermoelectric power factor. It also has an atypical shift from diamagnetism to paramagnetism with increasing temperature, and the fine details of its electron correlation effects have been widely discussed. The extraordinary physical properties must be rooted in the nature of the chemical bonding, and indeed, the chemical bonding in this archetypical marcasite structure has been heavily debated on a theoretical basis since the 1960s. The two prevalent models for describing the bonding interactions in $FeSb_2$ are based on either ligand-field stabilization of Fe or a network structure of Sb hosting Fe ions. However, neither model can account for the observed properties of $FeSb_2$. Herein, an experimental electron density study is reported, which is based on analysis of synchrotron X-ray diffraction data measured at 15 K on a minute single crystal to limit systematic errors. The analysis is supplemented with density functional theory calculations in the experimental geometry. The experimental data are at variance with both the additional single-electron Sb–Sb bond implied by the covalent model, and the large formal charge and expected *d*-orbital splitting advocated by the ionic model. The structure is best described as an extended covalent network in agreement with expectations based on electronegativity differences.

Introduction

More than a decade ago, $FeSb_2$ was discovered to be a narrow-gap semiconductor with strong electron correlations, making it a possible candidate for thermoelectric applications.[1,2] It was found to have a colossal low-temperature Seebeck coefficient (thermopower), S, of approximately $-45\,000\ \mu V K^{-1}$ at 10 K and an extremely large thermoelectric power factor, $S^2\sigma$, of around $2300\ \mu W K^{-1}$ at 12 K, in which σ is the electric conductivity.[3] Thermoelectric materials are able to interconvert thermal and electrical energy, and the thermoelectric figure of merit is defined as $zT = \sigma S^2 T/\kappa$, in which T is the absolute temperature and κ is the thermal conductivity. The thermal conductivity in $FeSb_2$ is too high to obtain a useful zT value, reducing it to 0.005 at 12 K[3], and considerable efforts have been directed toward lowering κ and potentially creating a new cryogenic cooling technology.[4] At low temperatures, $FeSb_2$ shows diamagnetic behavior, but with increasing temperature, the magnetic susceptibility gradually increases, in contrast to the isostructural $FeAs_2$, which remains diamagnetic.[5]

The origin of the extraordinary temperature dependence of the transport properties has been heavily debated,[6,7] and theoretical and experimental data suggest that they are linked to a combination of phonon-drag, electron-correlation effects, and anti-site defects to generate impurity in-gap electronic states. So far, no X-ray electron density (ED) analysis has been attempted to provide experimental evidence for the electronic structure.[8–10] As the ED imparts the physical properties of a system, it is clearly important to provide an understanding of the specific chemical bonding and atomic valence states in $FeSb_2$. However, the study of $FeSb_2$ by X-ray ED analysis is a great challenge because the structure contains heavy atoms, in which the valence electrons only contribute weakly to the diffracted intensities. An X-ray ED study of the similarly challenging thermoelectric material $CoSb_3$ has been reported[11,12] with a suitability factor, $S = V/\sum_{i,\text{unit cell}} n^2_{\text{core},i}$,[13] of 0.01, which is much lower than the values of 5–10 typically seen for organic compounds. Nevertheless, it was still possible to extract an accurate ED for $CoSb_3$. In the present case of $FeSb_2$, the suitability factor is 0.009, and this indeed makes it highly challenging to model the aspherical density features of the chemical bonds. Furthermore, dense inorganic crystal structures containing heavy atoms are more prone to systematic errors owing to extinction and absorption. However, this can be overcome by performing the X-ray diffraction experiments on a very small crystal and using short-wavelength synchrotron radiation. In addition, systematic errors caused by thermal diffuse scattering and anharmonicity can be reduced greatly by collecting data

[a] T. B. E. Grønbech, K. Tolborg, H. Svendsen, J. Overgaard, B. Brummerstedt Iversen
Center for Materials Crystallography
Department of Chemistry, and iNANO, Aarhus University
Langelandsgade 140, 8000 Aarhus C (Denmark)
E-mail: bo@chem.au.dk

[b] Y.-S. Chen
NSF's ChemMatCARS, The University of Chicago, Argonne, IL 60439 (USA)

Supporting information and the ORCID identification number(s) for the author(s) of this article can be found under: https://doi.org/10.1002/chem.202001643.

at very low temperatures by using helium cooling. In the following, in-depth descriptions of the crystal structure and proposed models are given.

The marcasite structure and chemical-bonding models

$FeSb_2$ belongs to the family of FeS_2 marcasite-type crystal structures. These binary compounds have the general formula MX_2, in which M is a transition metal and X is a group 15 or 16 element.[15] In general, they crystallize in the orthorhombic space group *Pnnm*.[16] The unit cell contains two formula units with M and X placed, respectively, at 2*a* (0,0,0) and 4*g* (*x*,*y*,0). The coordination environments are shown in Figure 1 for $FeSb_2$. Each X atom is coordinated in a distorted tetrahedral fashion by three M atoms and one X atom, and M is surrounded by six X atoms forming a distorted octahedron. One axis in the MX_6 octahedron is contracted, leading to two short axial M–X bonds and four longer equatorial M–X bonds. The angle between the bonds in the equatorial plane can deviate significantly from the ideal 90° of an octahedron. We will refer to this XMX angle between X atoms along the *c* direction as α, as illustrated in Figure 1 a. In the same direction the MX_6 octahedra form linear chains by sharing edges consisting of equatorial ligands. The tetrahedral angle XXM is approximately equal to the ideal tetrahedral angle. The remaining angles in the tetrahedron can deviate significantly from the optimal angle, with the MXM angle, in which X is bonded equatorially to both M, being equal to α by the linearity of the octahedral chain.[17]

Even though the whole family of MX_2 compounds is denoted marcasite, two distinct subgroups can be identified within this family, for which we follow the mineralogical naming convention of the *marcasites* and *löllingites*. The naming of the substructures is not consistent in the literature. Hullinger and Mooser named them anomalous and Jahn–Teller marcasites,[18] respectively, whereas Goodenough named them anomalous and regular marcasites.[17] To distinguish the main structure from the subgroups, we will refer to the main structure as the marcasite-type structure, and the subgroups as marcasite and löllingite. The subgroups are distinguished structurally by the unit cell ratios *c*/*a* and *c*/*b*. FeS_2 belongs to the marcasites with ratios close to 0.7 and 0.6 for *c*/*a* and *c*/*b*, respectively, whereas $FeSb_2$ belongs to the löllingites, with smaller ratios of 0.6 and 0.5, respectively.[16] A similar structural descriptor is the angle α, which is $<90^\circ$ for löllingites and $>90^\circ$ for marcasites. Correspondingly, the tetrahedral angle MXM spanning a chain is $<90^\circ$ in löllingites and $>90^\circ$ in marcasites, and consequently, the neighboring metal centers in the chain are relatively closer to each other in the löllingites.

From empirical studies, it appears that the substructures are linked to the number of *d* electrons on the metal ion. Assuming complete charge transfer, and that the cationic $(n+1)s$ orbital is higher in energy than the cationic *nd* orbitals, the population of the *nd* orbital can be extracted directly from the

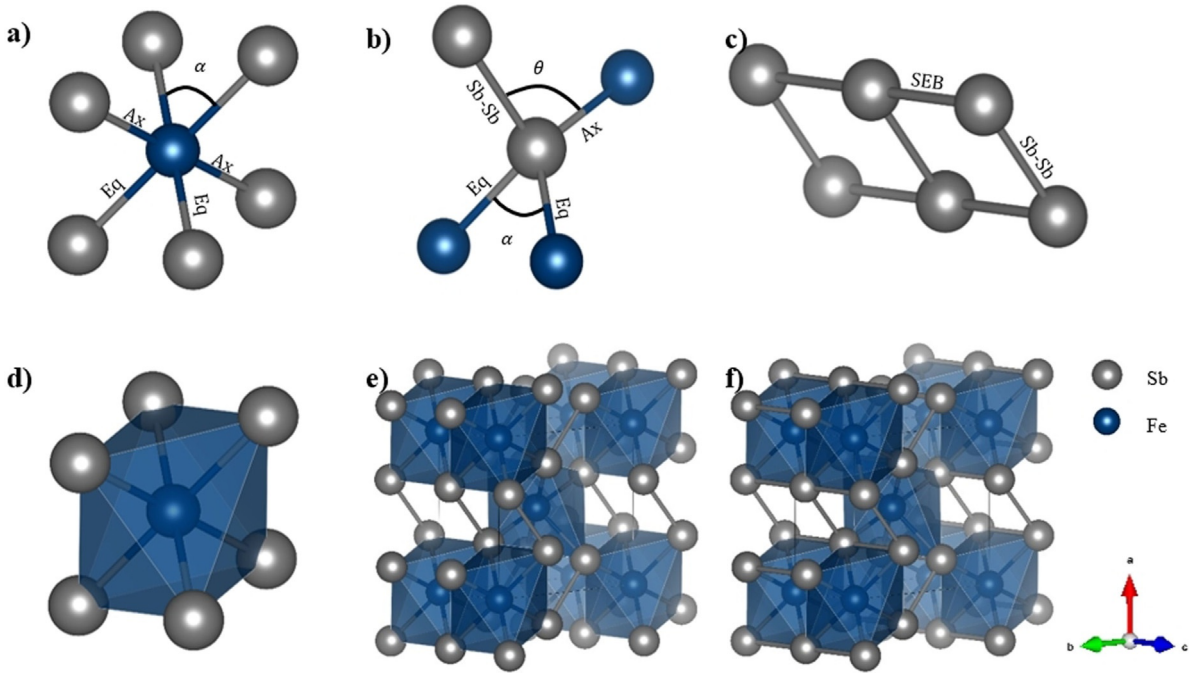

Figure 1. The local coordination around Fe (a) and Sb (b) in the $FeSb_2$ löllingite structure. The ladder proposed by Papoian and Hoffmann[14] is shown in (c). Ax and Eq denote the axial and equatorial Fe–Sb bonds in the distorted octahedron, α is the angle between equatorial Sb, θ is the tetrahedral XXM angle discussed in the main text, Sb–Sb is the conventional covalent bond, and SEB is the Single-Electron Bond proposed by Papoian and Hoffmann.[14] Note that the angle between equatorial and axial ligands in the $FeSb_6$ octahedron is only approximately 90° and that the value of θ depends on whether the central Sb is axially or equatorially bound to Fe, but in both cases is approximately 109.5°. Experimental values are included in Table S1, Supporting Information. The octahedral packing unit is shown in (d) with the same orientation as in (a), the conventional ligand-field-based structure is shown in (e), and the structure proposed by Papoian and Hoffmann[14] is shown in (f). The difference between the two structure depictions is the bond between Sb pairs along the *c* direction forming the ladder. Note that the equatorial ligands are shared between metal centers along the *c* direction.

metal's formal oxidation state. If the cation has six or more *d* electrons it will crystallize in the marcasite structure, whereas for four or fewer *d* electrons it will crystallize in the löllingite structure.[19] The FeS_2 marcasite structure is thus retained if S is replaced by any of the other group 16 elements. However, if a group 15 element substitutes for S as in $FeSb_2$, which is equivalent to removing two electrons per formula unit, the structure is converted into the löllingite type. Conversely, the marcasite structure is obtained if Fe is replaced by Ni in $FeSb_2$.

The original mechanism for the transition between the pyrite and marcasite structure family was proposed by Hullinger and Mooser.[20] They argued that the pyrite structure is formed for Jahn–Teller stable configurations in an octahedral field, whereas the marcasite structure is obtained for the Jahn–Teller unstable configurations. This is based on the proposed crystal-field splitting diagram in Figure 2, for which the closest similarity to an octahedral field is obtained for the pyrite structure. This mechanism, however, only accounts for a portion of compounds crystallizing in the marcasite structure,[21] and does not account for the substructure dependence on the electronic configuration or the reason why such substructures exist.

Following Hullinger and Mooser, Brostigen and Kjekshus observed that the löllingite-type structure can be obtained by a reorientation of half the anion pairs in the pyrite structure, that is, by changing the anion pair stacking sequence in the pyrite, further casting doubt on a Jahn–Teller stabilization mechanism.[22] They further argued that the difference between the löllingites and marcasites originates in the *d* orbital population following the crystal-field splitting scheme proposed by Hullinger and Mooser. The structural change is observed upon introducing the fifth *d* electron, which will populate the d_{xy} orbital, that is, the orbital directed toward nearest neighboring cations along the *c* direction giving rise to coulomb repulsion. The sixth electron will further repel the cation and no further change in the axial ratios are observed hereafter, consistent with the observed electronic configuration for the löllingites and marcasites.[19] Brostigen and Kjekshus also redetermined the space group to be *Pnn*2 by a Hamilton test,[21] although contemporary studies list it as the traditional *Pnnm*.[1,23] Petrovic et al.[23] did not observe any significant decrease in residuals by lowering the symmetry, and thus preferred the more symmetric space group.

This "expansion" model from löllingites to marcasites, however, ignores that the interactions between the d_{xy} orbitals would be favorable for $n \leq 5$, in contrast to its expected increase in axial ratios for $n = 5$ as pointed out by Goodenough.[17] Rejecting the cation–cation interaction, Goodenough instead proposed an expansion model based on cation–anion interactions.[17] The continually larger deviation of α from 90° will increase the overlap between the sp^3-hybridized anionic orbitals and the d_{xy} cationic orbital and reduce the overlap with the $d_{x^2-y^2}$ orbital. Assuming the orbitals on the anions are lower in energy than the cationic orbitals, this will destabilize the cationic d_{xy} orbital and stabilize the anionic orbital and cationic $d_{x^2-y^2}$. The fifth and sixth electrons will then occupy a destabilized cationic d_{xy} orbital, which is unfavorable, so α will tend back toward 90°, stabilizing the d_{xy} orbital and destabilizing the sp^3 and $d_{x^2-y^2}$ orbital. Without the stabilization of the anionic orbital associated with the löllingite structure, the marcasite structure is now energetically similar to the pyrite structure, which is why FeS_2 is found in both polymorphs.[17]

Assuming the Fermi energy (from filling with four *d* electrons) would fall between the occupied d_{xz}/d_{yz} orbitals and the unoccupied d_{xy} orbital with no orbitals in between, Goodenough's model is consistent with the electrical resistivity of $FeSb_2$ and $FeAs_2$. Both compounds are semiconducting and belong to the löllingite structure, but the bandgap in $FeAs_2$ is larger than that in $FeSb_2$. This is attributed to the larger splitting of the d_{xy} and d_{xz}/d_{yz} orbitals in $FeAs_2$ owing to a smaller α

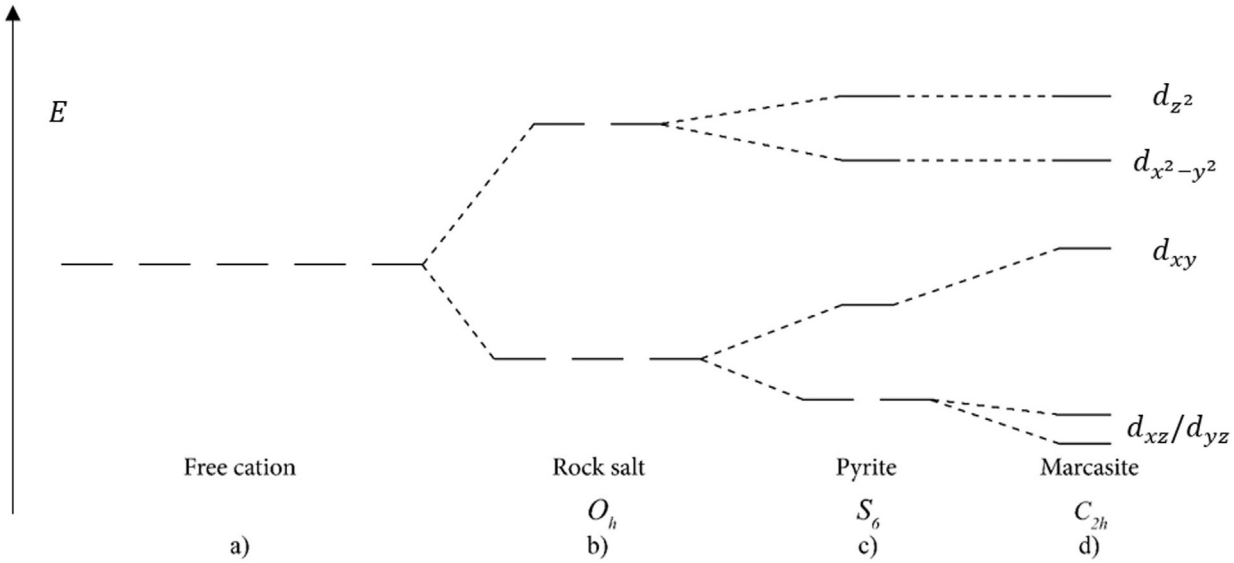

Figure 2. Energy diagram of the *d* orbitals for the central metal ion in different symmetries as originally proposed by Hullinger and Mooser.[20] Note that the splitting of the two highest-lying orbitals instead are degenerate in Goodenough's description of the pyrite structure.[17]

in this compound and less polarizable anion compared with $FeSb_2$.[24] The small gap in $FeSb_2$ makes it easier for electrons in the valence band, composed of the d_{xz}/d_{yz} orbitals, to enter the conduction band originating from overlapping d_{xy} orbitals on neighboring Fe atoms along the *c* axis. This in turn increases the magnetic susceptibility and electrical conductivity. The overlap along the *c* axis will allow for a possible anisotropy of physical properties in the *c* direction. Some studies have shown large anisotropy in the electrical resistivity with the highest conductivity along the *b* axis,[23] which is contrary to the expected, but this was not reproduced by Bentien et al.[1]

With Sb forming pairs, both Sb atoms fulfil their octet if the overall nominal charge of a pair is −4, leaving Fe with the exotic nominal charge of +4. However, the electronegativity difference between Fe and Sb is only 0.1 on the Pauling scale, making a complete charge transfer difficult to justify. Instead, the electronegativity supports another view of the bonding in $FeSb_2$ with formation of an infinite ladder by single-electron bond interactions between the Sb–Sb pairs along the *c* direction, as illustrated in Figure 1.[14] The existence of this additional bond reduces the charge on each Sb atom to −1, and thus, provides for a more conventional +2 state for Fe, consistent with the 18-electron rule as opposed to Goodenough's model. This suggests a d^6 configuration for Fe, with the two additional electrons occupying the d_{xy} orbital if the ordering scheme in Figure 2 is still valid. However, this model does not give a mechanism for the transformation between löllingite and marcasite structures, nor does it explain why $FeAs_2$ has a larger bandgap than $FeSb_2$.

Whether we embrace the ligand field bonding picture of Goodenough or the covalent ladder structure of Papoian and Hoffmann, none of the models are able to fully explain the physical properties of the family of marcasite-type structures. The above discussion shows that the formal valence state of Fe and the chemical bonding in the structure is unclear.

Results and Discussion

Three multipole electron density models have been refined; one on experimental data measured at the Advanced Photon Source (APS), and two on theoretical electron densities calculated using periodic density functional theory (DFT) in the experimental geometry and the functionals PBE[25] and mBJ[26] in the WIEN2k[27] code. For details see experimental section. The models will be referred to as APS, PBE, and mBJ, respectively.

Static electron deformation density

Model deformation densities are shown for three different multipole models (two theoretical, one experimental) in Figure 3 in selected planes to reveal the *d*-orbital splitting on Fe and the proposed single-electron bond proposed by Papoian and Hoffman.[14] On the former, all three models agree that the ED close to Fe is shifted away from the ligands toward the region of space corresponding to the d_{xz} and d_{yz} orbitals as seen in the first column, assuming the axial ligands lie on the local *z* axis of the metal center. This shift agrees with the energy splitting in Figure 2 assuming that Fe has four electrons. If Fe had six electrons, a charge accumulation would be expected in the equatorial plane (second column), assuming the orbitals are localized, which is not observed. The anisotropy of the charge depletion in the equatorial plane is opposite to the one expected from simple crystal-field theory, in which the largest depletion should be along the Fe–Sb bond. This is observed in all models, though the trend is clearer in the theoretical deformation densities. Still referring to Hullinger and Mooser's energy splitting diagram, this corresponds to changing the energy ordering of the $d_{x^2-y^2}$ and d_{xy} orbitals, indicating that covalency plays a more dominant role in the equatorial plane than expected. The experimental deformation density map also shows a shift of ED into a delocalized region along the Fe–Fe chains, which might indicate anisotropic properties as observed by Petrovic et al.,[23] but is not consistent with their observed orientations, and as such, the observed isotropy by Bentien et al.[1] seems more plausible. Furthermore, the experimental deformation density shows a shift of ED in between Fe and its equatorial ligands, whereas no significant change is observed between Fe and its axial ligand. For the theoretical deformations no significant accumulation of electron density is observed between Fe and its ligands.

Regarding the infinite ladder, the experimental deformation density is in disagreement with both the theoretical deformation densities. The experimental model removes ED in between the Sb pairs, but accumulates ED in the expected Sb–Sb bonds forming the dimers. The theoretical densities accumulate ED in the Sb–Sb dimer bond, but only mBJ also accumulates ED between dimer pairs, indicating the presence of Papoian and Hoffmann's single-electron bond forming the infinite ladder. For PBE, multiple changes of sign are instead observed in between Sb pairs, in disagreement with the presence of a covalent interaction, especially as the contour levels are separated by 0.01 e Å^{-3} and only the zero contour is observed to indicate a slight accumulation. Overall, the deformation density analysis leaves the validity of the Papoian and Hoffmann model unclear: the experimental data and PBE disagree with the ladder theory, whereas mBJ agrees. As we will show in the next section, no bond critical point is found for this interaction, suggesting no bonding interaction, in contradiction with the Papoian and Hoffmann model. Similar splitting of orbitals on Fe is seen in the Laplacian maps, and no charge concentration is seen between pairs of Sb dimers, indicating that no covalent interaction is present. These plots are included in Figure S5 (Supporting Information).

Bond critical points

The bond critical points (BCPs) are listed in Table 1 with their associated evaluated properties. The topological analysis is also performed directly on the theoretical EDs in WIEN2k. Only three distinct BCPs are found in all cases, consistent with the interactions described by Goodenough,[17] that is, there is no Sb–Sb interaction along the *c* direction and therefore no infinite ladder as proposed by Papoian and Hoffmann.[14] The

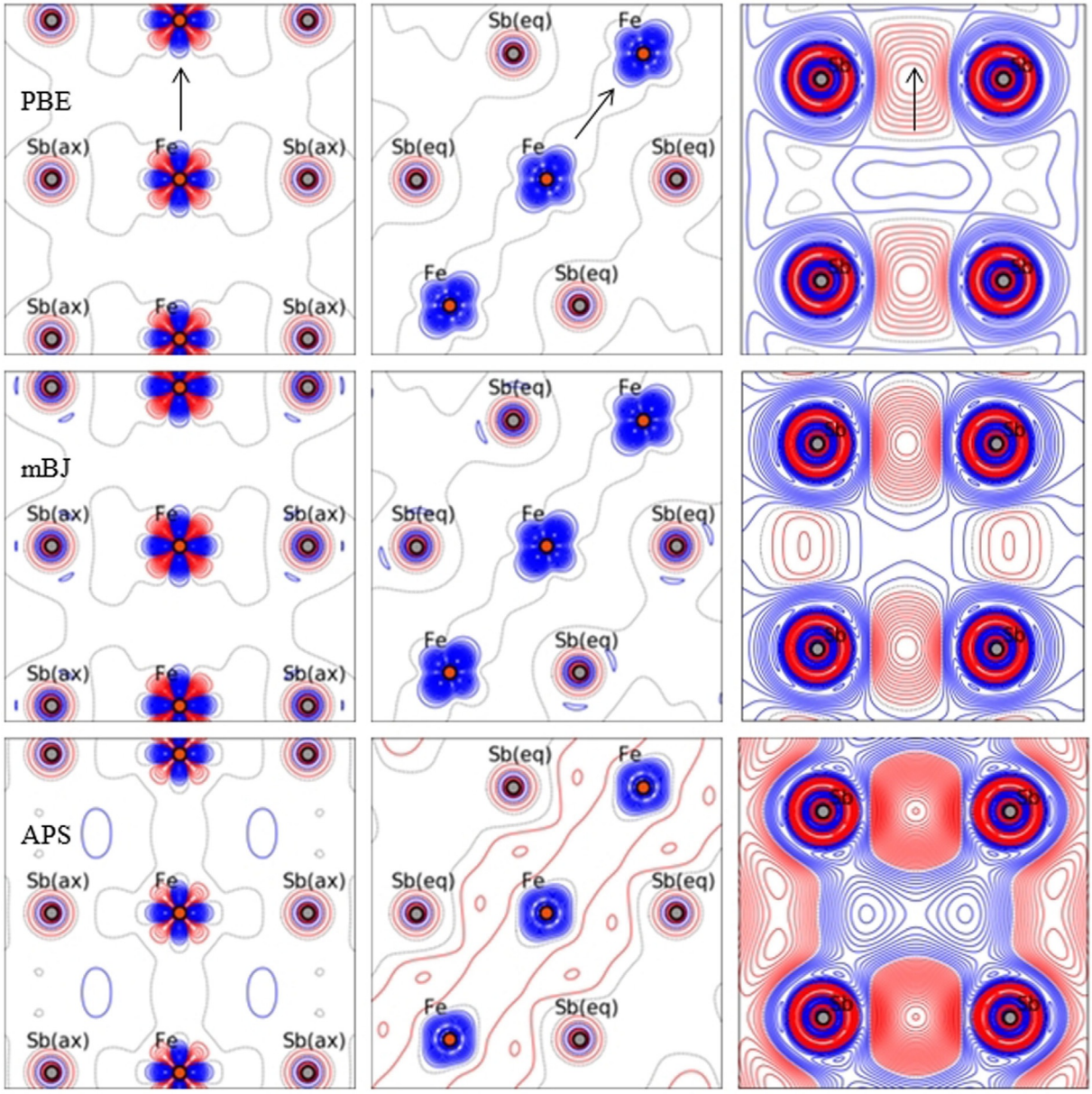

Figure 3. Deformation density in selected planes in the three models. Each row corresponds to a model in the order PBE, mBJ, and APS. Each column is a different plane. The arrows inserted in the first row correspond to the [001] direction. Fe together with its axial ligand is shown in the first column and with its equatorial ligands in the second column. The Sb–Sb ladder pairs are shown in the third column; horizontally the Sb pairs compose the rungs of the ladder, which extend in the vertical direction to form the ladder itself. The contour levels are 0.1 e Å^{-3} in the first and second columns and 0.01 e Å^{-3} in the third column. Positive, negative, and zero contours are marked with solid red lines, solid blue lines, and dotted black lines, respectively.

BCPs are distributed such that Sb interacts with one other Sb and three Fe atoms, and Fe interacts with six Sb atoms. Using only the sign of the Laplacian ($\nabla^2\rho$) as bond indicator would lead to the conclusion of Sb–Sb being a shared-shell interaction and both Fe–Sb bonds being closed-shell interactions, but, as pointed out by Macchi and Sironi,[28] this is a deceptive approach, especially for heavy elements. With the inclusion of the transition metals in the fourth period, the outer valence shell charge concentration (VSCC) is either missing (transition metals) or positive (some post-transition metals), whereby shared-shell interactions can have a positive $\nabla^2\rho$. This is related to the inherently diffuse *ns* orbitals for heavy elements and contracted $(n-1)d$ orbitals on transition metals.[29] Instead of evaluating $\nabla^2\rho$ only at the BCP, the whole bond path $\nabla^2\rho$-profile is evaluated (Figure 4) and the nature of the bonds are characterized by the energy densities as proposed by Macchi and Sironi.[28] Their classification of bonds, however, is mostly concerned with metal–metal (shared-shell) bonds and dative bonds for traditional coordination complexes with no heavy-element covalent bond description in solid networks, so the metal–metal bond will be used as proxy for comparison. The shared-shell interaction should not be confused with metallic bonding as expected in, for example, solid Fe, but is a covalent interaction in coordination complexes, meaning that it should

Table 1. Bond critical points found by topological analysis of the ED derived from multipole modelling of the experimental and theoretical structure factors. A direct analysis of the theoretical EDs in WIEN2k is included. The columns list the BCP in question, the model, the geometric distance between associated atoms, distance from atoms to BCP, and electron density, Laplacian, ellipticity, kinetic energy density, kinetic energy density per electron, potential energy density, and total energy density per electron at the BCP. All values are listed in atomic units except length, which is in Å; for example, the unit of kinetic energy density (G_b) is Hartree Å^{-3}. The energy densities are calculated by the Abramov approximation[30] and the local virial theorem. The listed uncertainty on $\nabla^2\rho$ is the one derived from XD, which is underestimated. $\nabla^2\rho$ is a rapidly changing function and even minor changes in the model and BCP position can alter its value drastically.[31–33]

BCP	Model	R	$d_{1\text{-BCP}}$	$d_{2\text{-BCP}}$	ρ_b	$\nabla^2\rho_b$	ε	G_b	G_b/ρ_b	V_b	H_b/ρ_b
Fe-Sb s	APS	2.5612	1.1661	1.3967	0.386(23)	1.549(21)	0.55	0.237	0.614	−0.365	−0.333
	PBE	2.5612	1.1557	1.4057	0.425(1)	1.454(1)	0.05	0.261	0.614	−0.420	−0.375
	PBE-WIEN2k	2.5612	1.1624	1.3988	0.417	1.207	0.02	0.243	0.584	−0.402	−0.381
	mBJ	2.5612	1.1497	1.4115	0.425(1)	1.403(1)	0.04	0.259	0.609	−0.419	−0.378
	mBJ-WIEN2k	2.5612	1.1274	1.4338	0.407	1.824	0.00	0.265	0.651	−0.402	−0.337
Fe-Sb l	APS	2.5929	1.1636	1.4452	0.524(20)	0.410(16)	1.36	0.293	0.559	−0.557	−0.504
	PBE	2.5929	1.1737	1.4203	0.375(0)	1.763(0)	0.16	0.239	0.638	−0.355	−0.308
	PBE-WIEN2k	2.5929	1.2080	1.3842	0.388	0.827	0.03	0.205	0.527	−0.352	−0.378
	mBJ	2.5929	1.1749	1.4197	0.373(0)	1.781(1)	0.25	0.239	0.640	−0.352	−0.305
	mBJ-WIEN2k	2.5929	1.1920	1.4019	0.382	1.013	0.03	0.209	0.547	−0.347	−0.362
Sb-Sb	APS	2.8814	1.4407	1.4407	0.507(22)	−1.768(26)	0.41	0.177	0.349	−0.477	−0.593
	PBE	2.8814	1.4407	1.4407	0.364(1)	0.339(1)	0.09	0.165	0.453	−0.306	−0.388
	PBE-WIEN2k	2.8814	1.4407	1.4407	0.381	−0.282	0.03	0.148	0.388	−0.316	−0.440
	mBJ	2.8814	1.4407	1.4407	0.404(1)	−0.237(1)	0.04	0.167	0.412	−0.350	−0.453
	mBJ-WIEN2k	2.8814	1.4407	1.4407	0.416	−0.931	0.02	0.143	0.343	−0.350	−0.500

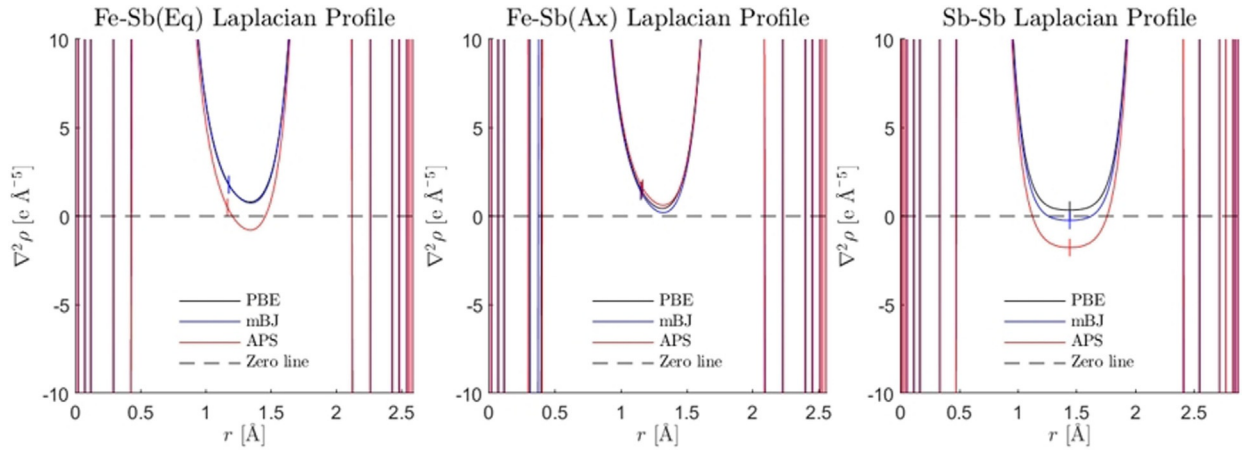

Figure 4. Laplacian profile along the bond path. Black is PBE, blue mBJ, and red APS. The dotted line represents a value of zero. The vertical lines indicate the BCP.

show similarities to general covalent bonds in solids of heavy elements.

All three types of interaction have a low kinetic energy per electron ($G_b/\rho_b < 1$) and have negative total energy per electron ($H_b/\rho_b < 0$), implying a dominance of potential energy at the BCP typical of shared-shell interactions. For the Sb–Sb interaction, $\nabla^2\rho$ is negative in all cases, but the MM projection of PBE is indicative of an ionic interaction. The changes in magnitude and sign of $\nabla^2\rho$ for this interaction by projecting the PBE ED onto the MM show how sensitive $\nabla^2\rho$ is to changes in the model, which is why the $\nabla^2\rho$ profile is more indicative of the nature of the bond. In all cases, the BCP is located at a minimum in $\nabla^2\rho$ equidistant from both Sb in a flat region consistent with metal–metal shared-shell interactions. The interaction differs from shared-shell covalent bonds of light elements by having the BCP at a local minimum instead of a local maximum in $\nabla^2\rho$. The lack of a maximum is linked to the diffuse 5*s* electrons, and as such, the interaction might be characterized as a proper covalent bond as expected from a homonuclear dimer ion. The magnitude of $\nabla^2\rho$ for the APS model is quite large for a heavy element interaction, and is probably linked to the noise present in the model as seen from the fractal dimension plots (Supporting Information).

Considering the Fe–Sb interactions, an increase in G_b/ρ_b and decrease in magnitude of H_b/ρ_b is observed compared with the Sb–Sb interaction. This implies a decrease in shared-shell character. Meanwhile, $\nabla^2\rho$ is positive in all cases and large in magnitude, indicative of a strong dative interaction or weak shared-shell interaction. However, the energy densities still indicate a degree of shared-shell interaction and the $\nabla^2\rho$ profiles show BCPs in somewhat flat regions of $\nabla^2\rho$. The Fe–Sb BCPs thus show characteristics of shared-shell interactions with a

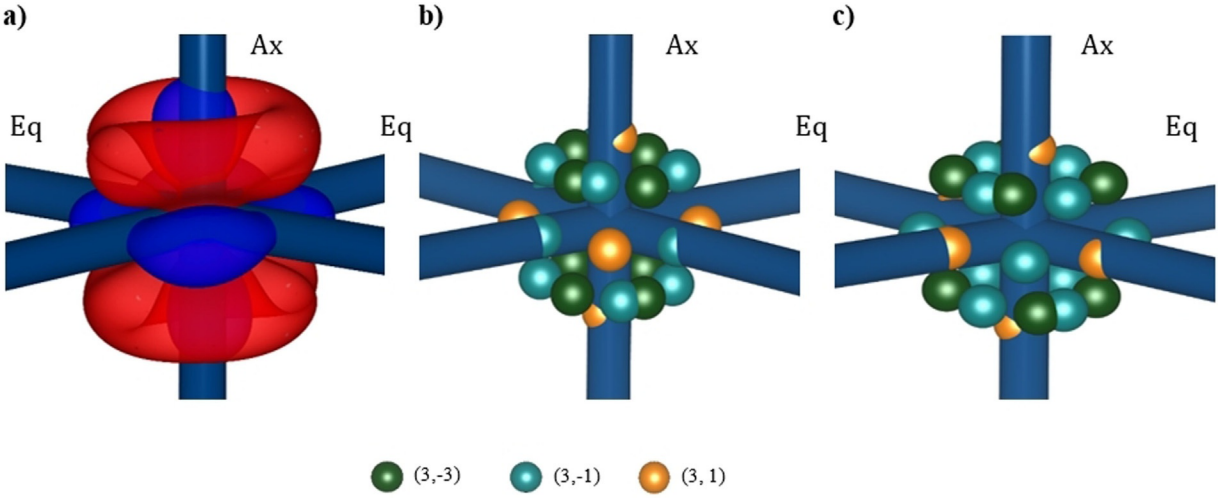

Figure 5. a) Isosurface of the deformation density at 0.03 e A^{-3} level. Red is positive and blue is negative. b) Critical points in $-\nabla^2\rho$ of the PBE model. The points are labeled by their rank and signature (*r,s*). Minima in the negative Laplacian, (3,3), are not included. Similar figures are found in Figure S6 (Supporting Information) for mBJ and APS, but the same conclusions can be drawn from these. c) As in (b) but with the CPs matching expectations from crystal-field theory.

degree of polarity. Note that the $\nabla^2\rho$ profile for the short Fe–Sb interaction is translated toward more positive $\nabla^2\rho$ compared with the longer interaction in the APS model, whereas the reverse trend is observed for the PBE and mBJ MMs. The former then predicts the equatorial bond to be more shared-shell than the axial, whereas the reverse is true for the latter. For the direct WIEN2k analyses, the value at the BCP increases on going from equatorial to axial, in line with the observation from APS. The discrepancy between MMs might be related to the position of the BCP and not actually the bond type, as the $\nabla^2\rho$ maps for all three models show the equatorial to be more covalent than the axial on the basis of charge concentrations in the *d* orbitals (vide infra).

In Figure 5 the deformation density isosurface is shown together with the (3,−3), (3,−1), and (3,1) critical points of $-\nabla^2\rho$ in the M-shell of Fe,[34] focusing on a single octahedron center. Note the close similarity between the deformation density lobes and the critical points. Interestingly, most charge is concentrated directly above and below the Fe–Sb(eq) plane. Following crystal field theory, the (3,−3) and (3,−1) CPs should be interchanged (see Figure 5 c) as this would give the largest charge concentration pointing the least toward Sb reducing the electrostatic repulsion. This is observed for the pyrites and marcasite.[35] In the present case, the largest charge concentration is bisecting the angle between Fe–Sb(eq) and Fe–Sb(ax), implying a degree of covalency. The remaining CPs do not follow the expected splitting in Figure 2 either, as the (3,−1) also lie within the equatorial bonds, whereas the (3,1) bisects the angle of these. The (3,1) CPs in the axial ligand bond do, however, adhere to the energy splitting diagram as these should be least populated. In general, all the points are rotated approximately 45° around the Fe–Sb(axial) bond compared with crystal field theory predictions, further indicating that the axial bond is more dative than the equatorial. This distribution of CPs indicates an inversion of the ordering of the d_{xy} and $d_{x^2-y^2}$ orbitals making the $d_{x^2-y^2}$ more stable as more charge is concentrated along the Fe–Sb(eq) bond compared with between the bonds.

d-orbital analysis

The derived *d*-orbital populations[36] are shown in Table 2. The coordinate system expected for the point group C_{2h} has not been used to calculate the populations. The reason is twofold: first, the coordinate system chosen by Goodenough[17] does not conform with the general choice, so to compare with his theoretical prediction, we have chosen to adopt the same coordinate system; and secondly, the chosen coordinate system reflects the deviation from octahedral symmetry better, whereby an easier comparison with the octahedron can be made, and thus, deviations from ligand-field theory expectations. The chosen coordinate system is shown in Figure 6. However, this coordinate system per construct will give symmetry-equivalent d_{xz} and d_{yz} orbitals as opposed to the energy splitting diagram in Figure 2. If the convention of assigning a coordinate system when a point group is given is followed then the energy splitting in Figure 2 is valid; however, the coordinate system chosen by Goodenough does not conform to the splitting

Table 2. *d*-orbital populations given in the coordinate system reflecting the chemical octahedral environment. The same coordinate system was employed by Goodenough.[17]

	F^{PBE}_{theory}	WIEN2k(PBE)	F^{mBJ}_{theory}	WIEN2k(mBJ)	F^{APS}
d_{z^2} [%]	16.8	16.1	15.0	14.0	17.3
$d_{x^2-y^2}$ [%]	19.9	19.5	20.2	19.7	19.5
d_{xy} [%]	16.9	16.5	15.8	15.2	18.1
d_{xz} [%]	23.2	24.0	24.5	25.5	22.6
d_{yz} [%]	23.2	24.0	24.5	25.5	22.6
total population [e]	6.042	6.361	6.241	6.383	5.91

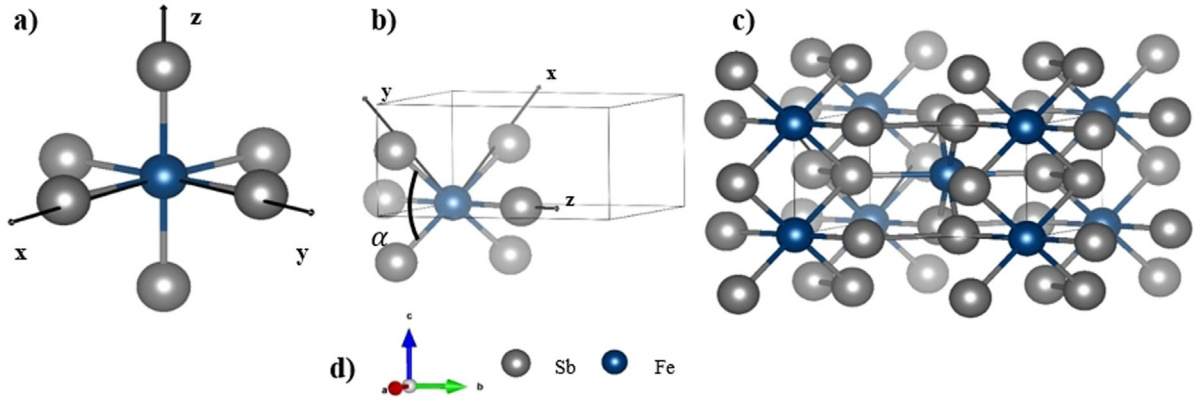

Figure 6. The chosen coordinate system reflecting the similarities to an octahedron (a) and embedded in the crystal structure (b and c). The crystallographic axes for (b) and (c) are shown in (d) together with a legend of atoms. Note that a mirror plane is present in the *ab* plane corresponding to the plane spanned by the vectors **z** and **x**−**y** forcing the d_{xz} and d_{yz} orbitals to be degenerate. This mirror plane is absent in Goodenough's orbital model. The point group coordinate system will have the *x* axis embedded in the mirror plane and the *y* axis perpendicular to it.

shown. This is reflected in the derived populations shown in Table 2. For all models, including the direct analysis of the ED, d_{xz} and d_{yz} are degenerate.

Comparing the derived populations in Table 2 with the ones in the coordinate system, minimizing the *d*-orbital cross-terms as proposed by Sabino and Coppens,[37] yields very similar values for orbitals having a *z* component. Minimizing the cross-terms leads to a more equal distribution in the purely *x*- and *y*-based orbitals, implying a rotation around the *z* axis essentially making the d_{xy} and $d_{x^2-y^2}$ orbitals degenerate. This is interesting in itself, and implies a degree of hybridization between these orbitals; however, we still choose to use the coordinate system employed by Goodenough to allow better comparison.

Interestingly, in contrast to Goodenough's model, the *d* orbitals on Fe accommodate roughly six electrons, and all the *d* orbitals are populated in all cases. However, in general, the method of calculating *d*-orbital populations from refined multipole coefficients by Holladay et al.[36] does not give empty orbitals as the MM parameters also account for covalent bonding effects, and as such, are not purely *d*-orbital related. This has similarly been observed in FeS_2 marcasite and pyrite.[35] Assuming there are actually six electrons and that they will occupy the three lowest orbitals at 0 K in Figure 2, the diamagnetic behavior is retained. However, the interaction cannot be explained fully in a crystal-field splitting picture with Sb_2^{4-} dimers coordinating with Fe^{4+}. The interaction must be more covalent with the oxidation state of Fe lowered to at least +II with the two additional electrons accommodated in the *d* orbitals participating in the covalent interaction.

This picture is further validated in the population order observed in Table 2. The d_{xz} and d_{yz} orbitals are the first to accommodate electrons, followed by $d_{x^2-y^2}$ and then d_{xy}, in contrast to the energy diagram in Figure 2. The $d_{x^2-y^2}$ orbital is the orbital pointing mostly toward the ligands in the equatorial plane, and its higher population compared to d_{xy} as such indicates that the *d*-orbitals in the *xy*-plane tend towards covalent interactions, the same trend seen for the charge accumulation/depletion in $\Delta\rho$ and charge concentrations in $\nabla^2\rho$. This would require an inversion of the $d_{x^2-y^2}$ and d_{xy} in the energy splitting diagram, requiring a stronger interaction between Fe and Sb than expected by Goodenough and with changes in α. Assuming the same *d*-orbital population for homologous compounds, this *d*-orbital inversion is still consistent with $FeAs_2$ having a larger bandgap than $FeSb_2$, as a smaller α will further destabilize the d_{xy} orbital, increasing the bandgap between itself and $d_{x^2-y^2}$, which to a first approximation is left unchanged. This idea is consistent with adding two electrons by substituting Fe with Ni, leading to the marcasite structure instead of the löllingite structure because these electrons will still occupy the destabilized d_{xy} orbital. This implies that the prediction of Brostigen and Kjekshus is not a switch between löllingites and marcasite with addition of the fifth and sixth *d* electrons, but rather the additional electrons from substituting the pnictogens with chalcogens will occupy the destabilized d_{xy} orbital, inducing a geometric rearrangement to the marcasite structure with d_{xy} lower in energy than $d_{x^2-y^2}$ as seen for marcasite FeS_2.[35]

The projected density of states (DOS) onto the *d* orbitals belonging to Fe of the theoretical densities are included in Figure 7. Note that a bandgap is present in the mBJ ED but it is missing in the PBE ED. Localized orbitals will, in general, give narrow bands, whereas delocalized electrons will give broad features in the DOS,[38] and in both EDs the d_{xz} and d_{yz} projections form narrow bands near the Fermi energy in the valence band and no significant features in the conduction band, in agreement with Goodenough's prediction of these being nonbonding and localized. The remaining orbital projections show a splitting of states with energies in both the valence and conduction bands. The d_{xy} orbital shows localized features in both the valence band and conduction band, whereas the $d_{x^2-y^2}$ and d_{z^2} orbitals show broad delocalized features in both bands. Near the Fermi energy in the valence band the $d_{x^2-y^2}$ band also shows a narrow peak signifying a degree of localization of this orbital.

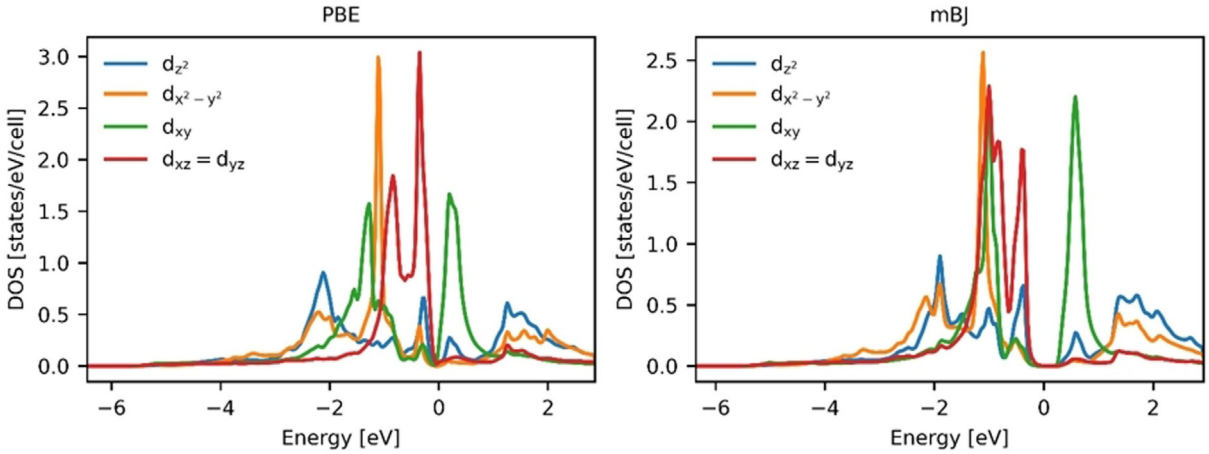

Figure 7. Projected density of states of the Fe *d* orbitals. The left figure is the DOS from PBE and the right is from mBJ.

This indicates that all three orbitals participate in bonding with Sb, whereas some $d_{x^2-y^2}$ and d_{xy} states are localized on Fe. The splitting of the d_{xy} orbitals into valence and conduction bands follows the mechanism described by Goodenough upon decreasing α, which should increase the interaction with the d_{xy}. This decrease in angle also decreases the interaction between $d_{x^2-y^2}$ and antimony's sp^3 orbitals, which is why localized features of the band appear in the valence band in contrast to pyrite, in which $\alpha \approx 90^\circ$, only having delocalized, split $d_{x^2-y^2}$ bands and localized d_{xy} orbitals.[35] Meanwhile, the conduction band minimum is composed mainly of d_{xy} orbitals. Forcing a localized picture on the ED around Fe with configuration $3d^6$ would then lead to the previously argued inversion of *d*-orbital population order, that is, the introduction of more electrons into the d_{xy} orbital is the destabilizing mechanism, not the introduction of electrons in the $d_{x^2-y^2}$ orbital. A localized description would then correspond to the splitting diagram in Figure 2 with these two orbitals switched.

The broad features in the valence band indicate that a localized description of the bonding/nonbonding states is not applicable, which initially contradicts the diamagnetic behavior at low temperature. The diamagnetism can be retained by considering that the d_{xz} and d_{yz} orbitals are mainly localized and located in the valence band. They can each accommodate two electrons with opposite spin, giving rise to diamagnetism. The remaining two electrons would be accommodated in the delocalized but filled orbitals, so the overall magnetic behavior would be diamagnetic at 0 K. The diamagnetism would progressively diminish at elevated temperatures as electrons would be excited into delocalized states and localized antibonding d_{xy} orbitals leaving behind unpaired spin.

Bader charges

The Bader charges, based on integrating the ED within atomic basins enclosed by the zero flux surface of the density as defined in Bader's Quantum Theory of Atoms In Molecules,[39] are listed in Table 3, together with the net charge of an $FeSb_2$ unit and the integrated Lagrangian. The non-zero net charge found in the MMs originates from numerical noise upon determining the zero flux surface and the basin integration itself. In all cases the models agree that the charge transfer is close to zero, and in all but one case the charge is transferred from Fe to Sb. The latter is in agreement with both Goodenough and Papoian and Hoffmann, but the former is in disagreement with both: Goodenough expected four electrons to be transferred to the Sb_2 unit, and Papoian and Hoffmann expected two electrons to be transferred to the Sb network. On the other hand, the observed almost zero charges on Fe and Sb are in agreement with expectations based on the nearly equal electronegativity of the atoms. Furthermore, the lack of charge transfer between atoms agrees with the previous observation in the ED, in which the interaction between Fe and Sb should properly be described as covalent and not ionic. Instead of considering the 3D crystal as units of ligand-field-stabilized octahedral and isolated dimers, it should be viewed as a covalent network with delocalized electrons.

Table 3. Bader atomic charges for Fe and Sb. The overall charge of a formula unit is included together with the integrated Lagrangian which should be as close to 0 as possible. For direct analysis of WIEN2k densities, the integrated Lagrangian is not reported, since the discontinuity at the muffin-tin surface introduces a non-zero contribution to the integral.[56]

Model		*O*(Fe)	*O*(Sb)	Q_{net}	*L*(Fe)	*L*(Sb)
APS	MM	0.07	0.00	0.07	8.6×10^{-3}	1.1×10^{-2}
PBE	MM	0.31	−0.13	0.05	2.9×10^{-3}	8.0×10^{-3}
	WIEN2k	−0.10	0.05	0.00	n/a	–
mBJ	MM	0.31	−0.12	0.07	2.7×10^{-3}	8.7×10^{-3}
	WIEN2k	0.11	−0.06	−0.01	n/a	–

The very small charge transfer is in contrast to the charge transfer observed in $CoSb_3$, for which both theory and experiment showed a significant negative (approximately −0.5 e) charge on Co.[11] However, this agrees very well with expectations from a recent scale of electronegativities based on average binding energies of valence electrons, placing Sb between Fe and Co, with Fe being the most electropositive element.[40]

Although it is not possible to predict the magnitude of charge transfer with the proposed electronegativities, they still replicate the direction of charge transfer.

Chemical bonding and transport properties

Electron density studies are inherently static. Dynamical aspects are incorporated through the Debye–Waller factor in the convolution approximation,[41] but this "thermal motion" factor does not relate directly to transport properties. Nevertheless, it would be highly desirable if correlations could be made between static chemical bonding features and specific transport properties. In studies of layered AB_2X_2 compounds in the $CaAl_2Si_2$ structure,[42] which include the very important thermoelectric material Mg_3Sb_2,[43,44] a strong correlation was found with the anisotropy of the thermal conductivity (κ), in which the ratio of the electron densities at intralayer and interlayer bond critical points ($\rho_{intra}/\rho_{inter}$) follow $\kappa_{intra}/\kappa_{inter}$ very closely.[45] The correlation basically established that the thermal conduction is large along covalent bonds. Similar correlations have been observed in ternary chalcogenides with stereochemically active lone pairs.[46] Here, materials with strongly expressed lone pairs have more covalent bond character and thus higher thermal conductivity. In a series of studies, Wuttig and coworkers have related chemical bonding features to various materials properties,[47] and introduced the term metavalent bonding for systems that are intermediate between metallic and covalent. Metavalent systems are typically observed to have good thermoelectric properties.[48] As the interactions in $FeSb_2$ are found to establish a covalent network structure, the thermal conductivity would be expected to be high, and this is indeed the case. In fact, it is the high thermal conductivity that has been the Achilles heel of $FeSb_2$ in relation to achieving a useful thermoelectric Figure of merit ($zT = TS^2\sigma/\kappa$), even though it has the highest known power factor ($S^2\sigma$) of any material.[3]

In the case of the electrical conductivity (σ), the general expectation is that a large density of delocalized electrons (large carrier concentration, high mobility) leads to a high σ. In early X-ray electron density studies, the peculiar non-nuclear maxima in the electron density of metallic beryllium were suggested as a signature of the excellent conduction properties.[49] In the present case, a purely ionic system with localized Sb dimers would not be expected to have a high electron mobility owing to the lack of orbital overlap, and would therefore have a low electrical conductivity. In the Zintl phase model of $FeSb_2$ proposed by Papoian and Hoffmann, the electrical conductivity would be enhanced by a high mobility in the Sb covalent network, but at the same time diminished by the low contribution of occupied Fe *d*-orbital states in the valence band as seen in Figure 7. It appears that the high electrical conductivity observed in $FeSb_2$ must arise from the covalent network formed by both Fe and Sb. Unfortunately, because the electrical and thermal conductivities are both linked to the covalent network, $FeSb_2$ does not decouple these transport properties and the desirable phonon-glass electron-crystal structure[50] in which the thermal conductivity can be tuned independently of the electrical conductivity cannot be adopted.

Conclusion

The two prevalent models for describing the bonding interactions in $FeSb_2$ are either based on ligand-field stabilization of Fe (Goodenough) or a network structure of Sb hosting Fe ions (Papoian and Hoffman). In the former model a large charge transfer between Fe and Sb is expected such that Fe exists in oxidation state +IV whereas the latter expects an additional single-electron bond between Sb atoms forming an infinite ladder structure. The ligand-field model further expects the Fe d_{xz} and d_{yz} orbitals to be occupied, with the remaining *d* orbitals empty and nondegenerate and the d_{xy} orbital lying lowest in energy. None of the features are found in the experimental multipole model, theoretical multipole models, or direct analysis of theoretical electron densities. There is no single-electron bond between Sb atoms, there is almost no charge transfer between Fe and Sb, more *d* orbitals are occupied, and, assuming the *d*-orbital populations are a valid indication of energetic ordering, the *d*-orbital ordering might not be that expected from ligand-field theory: the $d_{x^2-y^2}$ orbital is lower in energy than the d_{xy} orbital. This latter assumption, however, is only valid in the case of small to no covalent interaction. Staying within the restrictions on bonding interactions in ligand-field theory, however, aspects of Goodenough's model are consistent with the observed electron densities. Assuming six electrons in the Fe *d* orbitals with the observed ordering, d_{xy} will still be the lowest unoccupied orbital, with the destabilization of this orbital giving the löllingite structure and increasing occupancy giving the marcasite structure, as presented in the ligand-field model.

A ligand-field description is nevertheless not a sufficient description of the interactions as the Fe–Sb bonds do not appear to be dative interactions. On the other hand, the longer equatorial bond appears to be covalent with charge concentrations on both atoms pointing directly toward each other and a higher *d*-orbital population in the $d_{x^2-y^2}$ orbital compared with d_{xy} as a result of the covalency. The shorter axial bond does appear to have a larger degree of "dativeness" compared with the equatorial bond, consistent with the d_{z^2} orbital being the highest-energy orbital. However, with the charge transfer between Fe and Sb being close to zero, a "normal" dative interaction seems implausible. Both interactions are considered covalent with a larger degree of bond polarity in the axial interaction compared with the equatorial interactions, in line with expectations based on electronegativity.

The projected density of states for the Fe *d* orbitals show localized d_{xz}, d_{yz}, and d_{xy} orbitals, and the remaining are delocalized with $d_{x^2-y^2}$ showing a degree of localization near the Fermi level in the valence band. The $FeSb_2$ structure is then better described as a covalent network instead of ligand-field stabilized metal centers, both in relation to the band structure and small charge transfer, as well as the appearance of only covalent interactions.

Experimental Section

Single-crystal X-ray diffraction

X-ray diffraction data on a single crystal ($15\times25\times30$ μm) of $FeSb_2$, synthesized similarly to the approach adopted by Bentien et al.,[3] were collected at the NSF's ChemMatCARS, sector 15, at the Advanced Photon Source, USA. The data were measured with a Huber single-axis diffractometer equipped with a Bruker 6000 CCD detector. A helium cryostat (Pinkerton-type cooling device)[51] was used for cooling the crystal to approximately 15 K. The X-ray wavelength was 0.4428 Å. The data were integrated with *SAINT+*[52] and subsequently corrected for the oblique incident pathway through the CCD detector,[53] and frame scale factors were refined using *SADABS*.[52] Merging and absorption correction of the 9578 integrated reflections was performed using *SORTAV*,[54] providing a total of 1294 unique reflections ($R_{int}=0.028$). The linear absorption correction was $\mu=6.92$ mm^{-1} and the minimum and maximum transmissions were 0.829 and 0.848, respectively. The esd values from *SORTAV* were used as standard uncertainties in the refinements. The resolution of the data was 1.35 Å^{-1} and the overall completeness was 89.0%. A completeness of more than 99% was obtained up to 1.06 Å^{-1}. Three low-resolution reflections were missing owing to overexposure of the detector: (110), (120), and (031), of which the latter two are strong. The (110) reflection is very weak and was hidden by the beam stop. Only reflections measured at least three times (1006 reflections) were included in the refinements. An independent atom model refinement was performed with the program package *SHELXL*,[55] obtaining $R(F>4\sigma)=0.0179$.

Theoretical calculations

Density functional theory calculations were performed in the experimental geometry using the full-potential linear augmented plane wave plus local orbitals methods in the WIEN2k code.[27] Calculations using PBE[25] and mBJ[26] functionals as implemented in WIEN2k were performed. Reciprocal space was sampled at $11\times10\times21$ k grid with an $R_{MT}K_{max}$ of 10. The electron density inside the atomic spheres was expanded in spherical harmonics up to $l_{max}=10$, and the maximum l for partial waves used in calculations of non-muffin-tin matrix elements was 8. Muffin-tin radii (R_{MT}) of 2.41 bohr for both Fe and Sb were used. X-ray structure factors were calculated as a Fourier transform of the ED. Topological analysis of the direct theoretical density was performed with the CRITIC2 code.[56] Orbital projected density of states and total *d*-orbitals orbital populations in the rotated coordinate system were calculated based on the QTL subroutine of the WIEN2k code.

Electron density refinements

The EDs were modelled using the Hansen–Coppens Multipole Formalism[57] in the program package XD.[58] Unit weights were used in the refinement of theoretical data against *F*, whereas for the experimental data experimental weights and a lower bound of $I/\sigma(I)=3$ were used against F^2. Initial atomic positions and displacements parameters were refined using the high-order data with $\sin\theta/\lambda>0.8$ Å^{-1}. An isotropic extinction type I parameter with a Lorentzian distribution[59,60] was refined using all data. The tabulated atomic scattering factors were taken from the Volkov–Macchi data bank included in XD of relativistic STO wavefunctions with fitted single-ξ exponents based on the PBE functional. The atomic configurations used for Sb were $\{[Kr]4d^{10}\}5s^25p^3$ and for Fe were $\{[Ar]\}3d^6$ with the two 4*s* electrons on Fe added to the anion monopole parameter in the refinement to maintain electroneutrality. It is generally challenging to model the outermost *s* electrons on transition metals owing to their highly diffuse character, which leads to significant scattering contributions only in the innermost reflections. Furthermore, these reflections are also prone to extinction effects. In a similar study by Schmøkel et al.[35] on FeS_2, the Fe valence electrons were divided into two separate refinable valence populations, as in that case, moving the 4*s* electrons to the anion valence did not yield physically meaningful parameter values. In the present study, moving the 4*s* electrons to the anion valence resulted in stable refinements with reasonable parameter values, so we did not split the valence on Fe. Only a few multipole parameters for Fe and Sb are available (see Table S4, Supporting Information), restricted by the site symmetry of 2/*m* and *m*, respectively. The final model comprised two κ parameters on both Fe and Sb. It was, however, not possible to refine κ for Sb in the experimental data set owing to lack of convergence, as is often the case for this parameter. The κ parameters on both atoms were therefore locked at the values obtained from modelling the PBE theoretical structure factors. These structure factors gave the model with the smallest reliability factors as the VM-databank is based on PBE wavefunctions. The final datasets are limited to reflections $\sin\theta/\lambda\leq1.340$ Å^{-1} as large deviations between observed and calculated structures are observed above this value for the experimental dataset.

Multipole modelling of structure factors measured on a dense inorganic solid such as $FeSb_2$ contains many possible pitfalls, and it is important to scrutinize the accuracy of the corresponding electron density model. In the Supporting Information we present a detailed analysis of the final model, which shows it to be highly reliable.

Acknowledgements

This work was supported by the Villum Foundation and by Danscatt. Affiliation with the Center for Integrated Materials Research (iMAT) at Aarhus University is gratefully acknowledged. NSF's ChemMatCARS Sector 15 is supported by the Divisions of Chemistry (CHE) and Materials Research (DMR), National Science Foundation, under grant number NSF/CHE-1834750. Use of the Advanced Photon Source, a User Facility operated for the U.S. Department of Energy (DOE) Office of Science by Argonne National Laboratory, was supported by the U.S. DOE under Contract No. DE-AC02-06CH11357. The computational results were obtained at the Centre for Scientific Computing at Aarhus University.

Conflict of interest

The authors declare no conflict of interest.

Keywords: antimony · diamagnetism · marcasites · paramagnetism · semiconductors · thermopower

[1] A. Bentien, G. K. H. Madsen, S. Johnsen, B. B. Iversen, *Phys. Rev. B* **2006**, *74*, 205105.
[2] C. Petrovic, Y. Lee, T. Vogt, N. D. Lazarov, S. L. Bud'ko, P. C. Canfield, *Phys. Rev. B* **2005**, *72*, 045103.
[3] A. Bentien, S. Johnsen, G. K. H. Madsen, B. B. Iversen, F. Steglich, *Europhys. Lett.* **2007**, *80*, 17008.

[4] P. Sun, N. Oeschler, S. Johnsen, B. B. Iversen, F. Steglich, *Phys. Rev. B* **2009**, *79*, 153308.
[5] P. Sun, N. Oeschler, S. Johnsen, B. B. Iversen, F. Steglich, *Dalton Trans.* **2010**, *39*, 1012 – 1019.
[6] M. Battiato, J. M. Tomczak, Z. Zhong, K. Held, *Phys. Rev. Lett.* **2015**, *114*, 236603.
[7] J. M. Tomczak, *J. Phys. Condens. Matter* **2018**, *30*, 183001.
[8] K. Tolborg, B. B. Iversen, *Chem. Eur. J.* **2019**, *25*, 15010 – 15029.
[9] P. Coppens, *X-ray Charge Densities and Chemical Bonding*, Oxford University Press, Oxford, **1997**.
[10] V. R. Hathwar, M. Sist, M. R. V. Jørgensen, A. H. Mamakhel, X. Wang, C. M. Hoffmann, K. Sugimoto, J. Overgaard, B. B. Iversen, *IUCrJ* **2015**, *2*, 563 – 574.
[11] M. Stokkebro Schmøkel, L. Bjerg, J. Overgaard, F. Krebs Larsen, G. K. Hellerup Madsen, K. Sugimoto, M. Takata, B. Brummerstedt Iversen, *Angew. Chem. Int. Ed.* **2013**, *52*, 1503 – 1506; *Angew. Chem.* **2013**, *125*, 1543 – 1546.
[12] M. Stokkebro Schmøkel, J. Overgaard, B. Brummerstedt Iversen, *Z. Anorg. Allg. Chem.* **2013**, *639*, 1922 – 1932.
[13] E. D. Stevens, P. Coppens, *Acta Crystallogr. Sect. A* **1976**, *32*, 915 – 917.
[14] G. A. Papoian, R. Hoffmann, *Angew. Chem. Int. Ed.* **2000**, *39*, 2408 – 2448; *Angew. Chem.* **2000**, *112*, 2500 – 2544.
[15] H. Holseth, A. Kjekshus, *Acta Chem. Scand.* **1968**, *22*, 3273 – 3283.
[16] H. Holseth, A. Kjekshus, *Acta Chem. Scand.* **1968**, *22*, 3284 – 3292.
[17] J. B. Goodenough, *J. Solid State Chem.* **1972**, *5*, 144 – 152.
[18] F. Hulliger, E. Mooser, *Prog. Solid State Chem.* **1965**, *2*, 330 – 377.
[19] G. Brostigen, A. Kjekshus, *Acta Chem. Scand.* **1970**, *24*, 2993 – 3012.
[20] F. Hulliger, E. Mooser, *J. Phys. Chem. Solids* **1965**, *26*, 429 – 433.
[21] G. Brostigen, A. Kjekshus, *Acta Chem. Scand.* **1970**, *24*, 1925 – 1940.
[22] G. Brostigen, A. Kjekshus, *Acta Chem. Scand.* **1970**, *24*, 2983 – 2992.
[23] C. Petrovic, J. W. Kim, S. L. Bud'ko, A. I. Goldman, P. C. Canfield, W. Choe, G. J. Miller, *Phys. Rev. B* **2003**, *67*, 155205.
[24] A. K. L. Fan, G. H. Rosenthal, H. L. Mckinzie, A. Wold, *J. Solid State Chem.* **1972**, *5*, 136 – 143.
[25] J. P. Perdew, K. Burke, M. Ernzerhof, *Phys. Rev. Lett.* **1996**, *77*, 3865 – 3868.
[26] F. Tran, P. Blaha, *Phys. Rev. Lett.* **2009**, *102*, 226401.
[27] P. Blaha, K. Schwarz, F. Tran, R. Laskowski, G. K. H. Madsen, L. D. Marks, *J. Chem. Phys.* **2020**, *152*, 074101.
[28] P. Macchi, A. Sironi, *Coord. Chem. Rev.* **2003**, *238 – 239*, 383 – 412.
[29] C. Gatti, *Zeitschr. Krist.- Cryst. Mater.* **2005**, *220*, 399 – 457.
[30] Y. A. Abramov, *Acta Crystallogr. Sect. A* **1997**, *53*, 264 – 272.
[31] R. Kamiński, S. Domagała, K. N. Jarzembska, A. A. Hoser, W. F. Sanjuan-Szklarz, M. J. Gutmann, A. Makal, M. Malińska, J. M. Bąk, K. Woźniak, *Acta Crystallogr. Sect. A* **2014**, *70*, 72 – 91.
[32] B. Fournier, B. Guillot, C. Lecomte, E. C. Escudero-Adán, C. Jelsch, *Acta Crystallogr. Sect. A* **2018**, *74*, 170 – 183.
[33] M. W. Shi, S. P. Thomas, V. R. Hathwar, A. J. Edwards, R. O. Piltz, D. Jayatilaka, G. A. Koutsantonis, J. Overgaard, E. Nishibori, B. B. Iversen, M. A. Spackman, *J. Am. Chem. Soc.* **2019**, *141*, 3965 – 3976.
[34] Z. Shi, R. J. Boyd, *J. Chem. Phys.* **1988**, *88*, 4375 – 4377.
[35] M. S. Schmøkel, L. Bjerg, S. Cenedese, M. R. V. Jørgensen, Y.-S. Chen, J. Overgaard, B. B. Iversen, *Chem. Sci.* **2014**, *5*, 1408 – 1421.
[36] A. Holladay, P. Leung, P. Coppens, *Acta Crystallogr. Sect. A* **1983**, *39*, 377 – 387.
[37] J. R. Sabino, P. Coppens, *Acta Crystallogr. Sect. A* **2003**, *59*, 127 – 131.
[38] J. B. Goodenough, *J. Appl. Phys.* **1966**, *37*, 1415 – 1422.
[39] R. F. W. Bader, *Atoms in Molecules: A Quantum Theory*, Clarendon, Oxford, **1994**.
[40] M. Rahm, T. Zeng, R. Hoffmann, *J. Am. Chem. Soc.* **2019**, *141*, 342 – 351.
[41] W. F. Kuhs, *Acta Crystallogr. Sect. A* **1992**, *48*, 80 – 98.
[42] J. Zhang, L. Song, B. B. Iversen, *NPJ Comput. Mater.* **2019**, *5*, 1 – 17.
[43] J. Zhang, L. Song, S. Pedersen, H. Yin, L. T. Hung, B. B. Iversen, *Nat. Commun.* **2017**, *8*, 13901.
[44] J. Zhang, L. Song, G. K. H. Madsen, K. F. F. Fischer, W. Zhang, X. Shi, B. B. Iversen, *Nat. Commun.* **2016**, *7*, 10892.
[45] J. Zhang, L. Song, M. Sist, K. Tolborg, B. B. Iversen, *Nat. Commun.* **2018**, *9*, 4716.
[46] K. Tolborg, C. Gatti, B. B. Iversen, *IUCrJ* **2020**, *7*, 480 – 489.
[47] J. Y. Raty, M. Schumacher, P. Golub, V. L. Deringer, C. Gatti, M. Wuttig, *Adv. Mater.* **2019**, *31*, 1806280.
[48] M. Cagnoni, D. Fuhren, M. Wuttig, *Adv. Mater.* **2018**, *30*, 1801787.
[49] B. B. Iversen, F. K. Larsen, M. Souhassou, M. Takata, *Acta Crystallogr. Sect. B* **1995**, *51*, 580 – 592.
[50] G. J. Snyder, M. Christensen, E. Nishibori, T. Caillat, B. B. Iversen, *Nat. Mater.* **2004**, *3*, 458 – 463.
[51] M. J. Hardie, K. Kirschbaum, A. Martin, A. A. Pinkerton, *J. Appl. Crystallogr.* **1998**, *31*, 815 – 817.
[52] L. Krause, R. Herbst-Irmer, G. M. Sheldrick, D. Stalke, *J. Appl. Crystallogr.* **2015**, *48*, 3 – 10.
[53] G. Wu, B. L. Rodrigues, P. Coppens, *J. Appl. Crystallogr.* **2002**, *35*, 356 – 359.
[54] R. H. Blessing, *J. Appl. Crystallogr.* **1997**, *30*, 421 – 426.
[55] G. M. Sheldrick, *Acta Crystallogr. Sect. C* **2015**, *71*, 3 – 8.
[56] A. Otero-De-La-Roza, E. R. Johnson, V. Luaña, *Comput. Phys. Commun.* **2014**, *185*, 1007 – 1018.
[57] N. K. Hansen, P. Coppens, *Acta Crystallogr. Sect. A* **1978**, *34*, 909 – 921.
[58] A. Volkov, P. Macchi, L. J. Farrugia, C. Gatti, P. R. Mallinson, T. Richter, T. Koritsanszky, XD2016-A Computer Program Package for Multipole Refinement, Topological Analysis of Charge Densities and Evaluation of Intermolecular Energies from Experimental or Theoretical Structure Factors, **2016**.
[59] W. H. Zachariasen, *Acta Crystallogr.* **1967**, *23*, 558 – 564.
[60] P. J. Becker, P. Coppens, *Acta Crystallogr. Sect. A* **1974**, *30*, 129 – 147.
[61] E. D. Stevens, M. L. Delucia, P. Coppens, *Inorg. Chem.* **1980**, *19*, 813 – 820.

Manuscript received: February 20, 2020
Accepted manuscript online: April 16, 2020
Version of record online: June 22, 2020